

Numerical Simulation of Alumina-Mixing Process with a Multicomponent Flow Model Coupled with Electromagnetic Forces in Aluminum Reduction Cells

HONGLIANG ZHANG,¹ SHUAI YANG,¹ HEHUI ZHANG,¹ JIE LI,^{1,2}
and YUJIE XU¹

1.—School of Metallurgy and Environment, Central South University, No. 932, Lushan South Road, Changsha 410083, People's Republic of China. 2.—e-mail: csulijie@126.com

An extended computational fluid dynamics model combined with the driving forces of anode gas bubbles and electromagnetic forces (EMFs) was developed for the alumina-mixing process in aluminum reduction cells. A practical feeding scheme and the consuming rate of alumina depending on the local current intensity of the bath–metal interface were considered in the simulation. A comparative numerical study was carried out using the models with and without considering the EMFs. The results show that considering different driving forces in modeling can lead to different results for alumina mixing in the cell. The existence of the bubble movement makes alumina disperse more quickly in local areas, and it greatly contributes to the vertical dispersion in the early stage of mixing. The EMF plays a more important role in the long-range transportation of alumina in the cell. Both forces should be taken into consideration in the modeling because they have a positive influence on distribution uniformity and the dispersion rate of alumina.

INTRODUCTION

Alumina is the primary raw material for aluminum production in the Hall–Héroult cell (Fig. 1), which is consumed in the electrochemical reduction process. After adding into electrolyte (bath) from several hoppers, alumina undergoes a series of complex physical and chemical processes, including heating, dissolution, and mass transfer. Finally, it gets reduced on the metal–bath interface.¹ As the local superheat and electrical resistivity of the bath strongly depend on the local alumina concentration, it is of great benefit to the cell performance and current efficiency when alumina gets evenly dispersed.^{2–4} Moxnes et al.⁵ showed that a more uniform alumina distribution can improve current efficiency and reduce abnormal operating conditions, such as anode effect (AE), cell voltage oscillation, and emission of greenhouse gases. In contrast, if local alumina concentration gets too high, the cell productivity could be reduced, and solidification and settlement of sludge⁶ could also occur because the newly added alumina cannot be dissolved efficiently and timely. This would lead to

an uneven temperature and electromagnetic distribution that are undesirable in the production. Besides, although there are controversial aspects in the mechanism of AE, it is commonly known that a low local alumina concentration in the bath is the major cause.⁷ An AE normally starts at the anode region with the lowest alumina concentration and spreads to the other anodes.⁸

To obtain an even distribution of alumina concentration, it is necessary to investigate the mixing process of alumina; thus, a more precise control of alumina dissolution and distribution can be possible. For industrial aluminum reduction cells, the bath temperature and the source of alumina are maintained in a stable technological condition, so that the circulatory motion of bath plays a dominant role in the mixing process. Because of the strong corrosiveness and high temperature of the bath, it is very difficult to directly measure the distributions of bath flow and alumina concentration. Rye et al.⁹ used the anode current distribution to determine the transfer path of bath flow by tracing the anode current variations after adding a large quantity of aluminum fluoride to the bath at different feeder

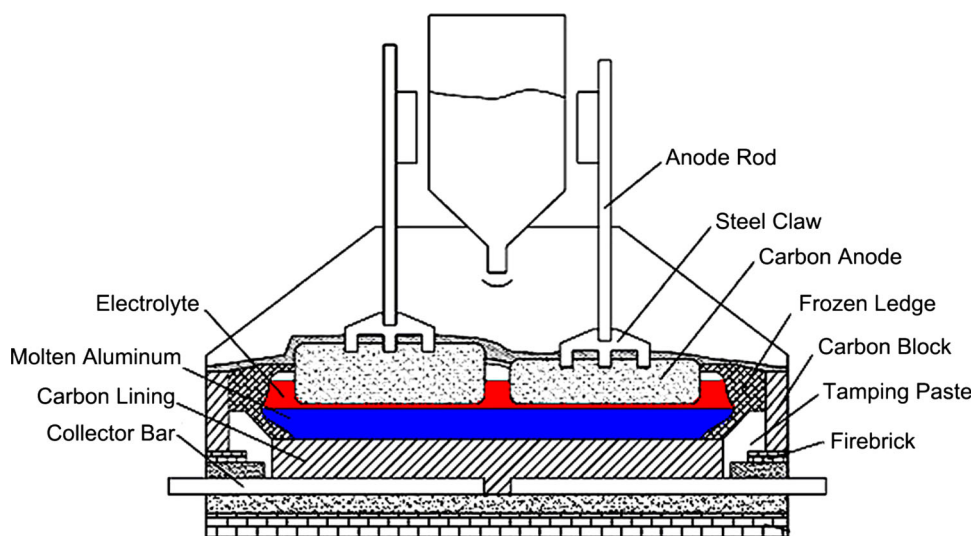


Fig. 1. Cross section of a modern aluminium reduction cell.

locations; however, few details were discussed in their publications. Thus, physical modeling and computational fluid dynamics (CFD) modeling have been the primary methods in studying and optimizing the melt flow field. It is reported that the fluid flow-related phenomena such as mass transport and heat-transfer processes in the electrolysis cell are dominated by the magneto-hydrodynamic (MHD),^{10–12} gas-driven,¹³ and thermal-gradient-driven forces.¹⁴ Besides, according to the observation and mathematical simulation by Wang et al.,¹⁵ the design and operation of the anode also have considerable effects. However, the alumina mixing was not precisely studied as the properties of alumina particle and electromagnetic forces (EMFs) were difficult to take into consideration. Chesonis et al.¹⁶ studied the influence of bath flow on alumina distribution in a 90-kA aluminum reduction cell with a water–air physical model by using sodium chloride to trace the mixing process of alumina. They found that anode bubbles play a more important role than EMFs in the mixing of alumina. However, the conclusion still needs to be confirmed because the EMFs cannot be simulated correctly by the method of pumping water from the end side in physical model. Feng et al.^{17,18} presented a transient CFD model to calculate the alumina concentration distribution in bubble-driven flow under different feeding strategies and cell structures, but they also neglected the influence of EMFs in their model. Nonetheless, the effect of EMFs proved to play an important role in bath flow in many studies.^{19–21} Nowadays, the current intensity of the newly built cells has generally increased to as high as 300 kA or more, which makes the EMFs become one of the decisive factors for alumina concentration distribution. Actually, according to Kobbeltvedt et al.,²² alumina was obviously transferred largely to upstream side because of the asymmetry of EMFs. This means the model proposed in Refs. 17

and 18 may be unsatisfactory, judging from the strictly symmetric alumina concentration distributions under any conditions.

This article presents a multiphase CFD modeling of the alumina-mixing process that considers the influence of the electromagnetic field. It introduces the method of considering the EMFs and the consuming rate of alumina, which depends on the local current intensity of the bath–metal interface. This model provides a more precise prediction of the alumina concentration distribution and its time-varying characteristics. Moreover, to determine the primary factors that influence the distribution of alumina concentration, the individual effect of bubbles or EMFs on the above process are also studied, respectively.

THEORETICAL MODEL

Pseudo-homogeneous Hypothesis and Some Simplifications

Although alumina has both solid particle and fluid characteristics during the mixing process, much attention is paid to its fluid behavior. Hence a pseudo-homogeneous model of bath was proposed, which assumes the bath as a single phase consists of two components, molten cryolite and alumina. Thus, the mixing process of alumina can be simulated by the multicomponent flow model.

In addition, the following simplifications were put forward:

1. The bath was regarded to be incompressible and isothermal flow, and the ledge shape was invariant.
2. The anode base was flat and anode–cathode distance (ACD) was constant.
3. The metal layer was neglected, so the bottom of the bath could be regarded as the bath–metal interface (cathode).

4. The bubbles were present as particles with equivalent diameter, so the bubble phase could be treated as a dispersed phase.

The Governing Equations

In this work, the time-averaged Navier–Stokes equations were solved based on the Euler/Euler approach to predict the three-dimensional (3-D) transient bath-gas flow. The continuity and momentum equations can be written as follows, respectively:

$$\frac{\partial}{\partial t}(r_\alpha \rho_\alpha) + \nabla \cdot (r_\alpha \rho_\alpha U_\alpha) = 0 \quad (1)$$

$$\begin{aligned} \frac{\partial}{\partial t}(r_\alpha \rho_\alpha U_\alpha) + \nabla \cdot (r_\alpha (\rho_\alpha U_\alpha \times U_\alpha)) = -r_\alpha \nabla P_\alpha \\ + \nabla \cdot (r_\alpha \mu_{\alpha \text{eff}} (\nabla U_\alpha + (\nabla U_\alpha)^T)) + S_{M_\alpha} + M_\alpha \end{aligned} \quad (2)$$

where r_α , ρ_α , U_α , P_α , and $\mu_{\alpha \text{eff}}$ are the volume fraction, density, velocity, pressure, and effective viscosity of phase α , respectively; M_α represents the interphase drag force on phase α due to the bubble motion (other interfacial interphase forces are neglected); and S_{M_α} represents the momentum sources caused by external body forces, such as EMFs and buoyancy for this study. Besides, with the bath and bubble set to be phase 1 and phase 2, respectively, the volume fraction sums to unity:

$$\sum_{\alpha=1}^2 r_\alpha = 1 \quad (3)$$

In Eq. 2, the interphase drag force depends on the drag coefficient and the interfacial area density. And the momentum sources in the whole fluid region can be set by introducing the 3-D EMFs, which is the cross product of electric current density and magnetic induction intensity that are the results of the electromagnetic coupled model. The details for calculating the interphase drag force and obtaining the distribution of EMFs can be found in our earlier studies.^{19,23}

For the bath phase (phase 1), it is essential to note the mass conservation equation of each component, namely the transportation equation of alumina:

$$\frac{\partial}{\partial t}(r_1 \rho_1 Y_{\text{Al}}) + \nabla \cdot (r_1 (\rho_1 U_1 Y_{\text{Al}} - r_1 D_{\text{Al}} (\nabla Y_{\text{Al}}))) = S_{\text{Al}} \quad (4)$$

Equation 4, from left to right, shows are the varying term, convection term, diffusion term, and source term of alumina, where Y_{Al} and D_{Al} are, respectively, the mass fraction and kinematic diffusivity of alumina in bath, and S_{Al} describes the mass source, which includes the feeding and

electrochemical consumption of alumina. As a constraint equation, the sum of mass fraction of alumina and cryolite always equals 1.

Calculation of the Mass Source of Alumina

The Feeding of Alumina

Alumina was added to the bath from the feeding hoppers in a regular interval. A positive time-varying mass source term was built in each feeding region to simulate the feeding process of alumina. In a normal circumstance, there is a time lag in the alumina mass change caused by the heating and sintering process, which delays alumina to escape from the feeding region and disperse into the bath bulk. If the time lag of mass source is τ and the escape time is δ , then the time-varying mass source function of alumina can be written as follows:

$$f(t) = \lambda \cdot \frac{T m_0}{n \delta} \cdot \text{step}\{\sin[\omega(t + q - \tau)] - \sin(\omega q)\} \quad (5)$$

where m_0 , T , and λ are the consumption rate of alumina, feeding interval, and coefficient of feeding amount ($\lambda > 1$ for overfeeding and $\lambda < 1$ for underfeeding) respectively, and ω and q are the frequency and left shift of the sine function respectively.

$$\omega = \frac{2\pi}{T} \quad (6)$$

$$q = \frac{T}{4} - \frac{\delta}{2} \quad (7)$$

The function “*step()*” is a step function. It returns to 1 if the independent variable is greater than 0, or else it returns to 0.

The Electrochemical Consumption of Alumina

Based on the law of mass conservation, the consumption rate of alumina was determined by the production rate of aluminum, which can be calculated by the local current density at the bottom of the bath. Consequently, the local consumption rate of alumina m_{loc} ($\text{kg s}^{-1} \text{m}^{-2}$) can be written as:

$$m_{\text{loc}} = \frac{17}{32400} \cdot K J_b \eta \quad (8)$$

where K is electrochemical equivalent of aluminum ($0.3356 \text{ g A}^{-1} \text{ h}^{-1}$), J_b is local current density at the bath bottom (A m^{-2}), and η is the current efficiency of the cell. Hence, with the current density distribution, the distribution of m_{loc} can be induced as negative source mass.

Turbulence Model and Boundary Condition

Considering the different physical properties and flow behaviors of the bath and bubble, the

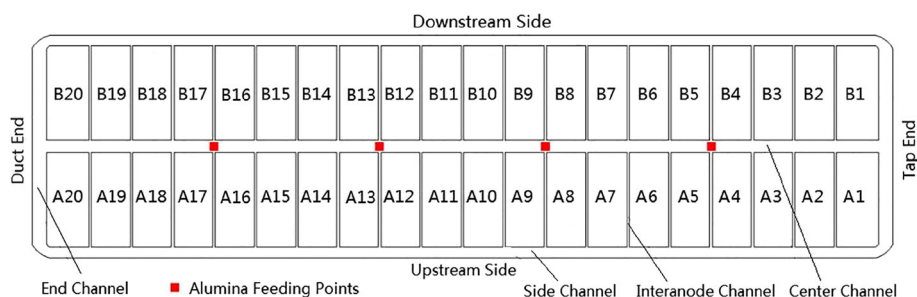


Fig. 2. Sketch map for full scale computational region in 300-kA cell.

multiphase flow can be solved with fluid-dependent model. A $k-\varepsilon$ turbulence model and a zero-equation turbulent model were applied in the bath phase and the bubble phase, respectively. All the faces of the fluid region were set as no-slip walls with wall function of turbulence equations for bath except the top face, which was regarded to be free-slip wall to allow the wave of bath. For the bubble phase, the inlet boundaries were built on the anodes surfaces and an outlet boundary was adopted on the top face, whereas the rest faces were treated as free-slip walls. Therefore, after gas bubbles are released from the anode surfaces, they will move through the channel and flow over the ledge without any friction. Once they reach the top face, they will escape and the computation for the bubble phase will be terminated. The generation rate of the bubble q_{loc} ($\text{kg s}^{-1} \text{m}^{-2}$) can be calculated by the following expression:

$$q_{loc} = \frac{J_a(22a + 14b)}{10^3 F(2a + b)} \quad (9)$$

where a and b are the volume percentage of CO_2 and CO in anode gas, respectively; J_a is local current density on the anode surfaces (A m^{-2}); and F is Faraday constant (96485 C mol^{-1}). Considering that the industrial current density is around 0.8 A cm^{-2} , the mean diameter of bubbles was approximately taken as 10 mm according to the physical modeling results made by Cassayre et al.²⁴

APPLICATION CASE AND NUMERICAL ANALYSIS

Case Examined

The study object of this article was a 300-kA aluminum reduction cell with 20×2 prebaked anodes. Because of the asymmetric feature of the flow field, a full-scale bath motion region with the volume of $14.64 \text{ m} \times 3.84 \text{ m} \times 0.44 \text{ m}$ was calculated. The ACD is 0.045 m, and the widths of the interanode channel, the side one, the center one, and the end one are 0.04 m, 0.22 m, 0.20 m, and 0.31 m, respectively. There are four alumina feeding regions of $0.16 \text{ m} \times 0.16 \text{ m} \times 0.02 \text{ m}$ evenly distributed in the center channel, and the top of each region was set at the bath surface. For simplicity, only the

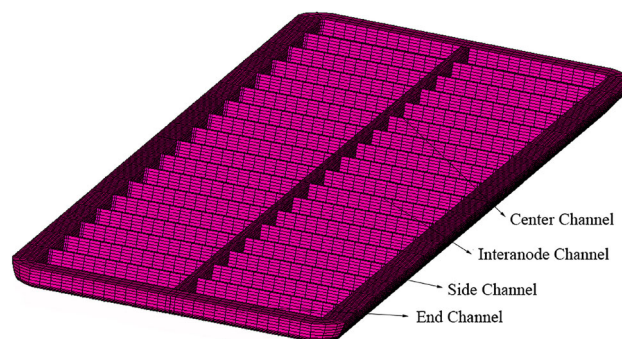


Fig. 3. The computational mesh of the 300-kA cell.

normal feeding mode was considered with the feeding interval fixed as 60 s. A schematic diagram of the cell with numbered anodes is shown in Fig. 2.

Numerical Method

The commercial CFD code CFX was used to carry out the calculation with the computational mesh, shown in Fig. 3, containing 455488 elements and 385810 nodes. For the transient numerical solution, a proper initial value is of great importance to ensure the accuracy of each time step. Hence a steady-state flow field result was given as the initial condition and the initial alumina concentration was specified as 2.5 wt.% in the whole region.

The SIMPLE algorithm was used for the transient iterative process. The maximum coefficient loop was set to be 10 for the timescale control, and the root mean square residual target of less than 10^{-4} was adopted for convergence.

RESULTS AND DISCUSSION

The Predicted Distributions of Consumption Rate of Alumina and Velocity

The distribution of consumption rate of alumina is shown in Fig. 4. On the whole, the distribution is obviously inhomogeneous. The consumption rate in the upstream side is a little higher than that in the downstream side, and it is also higher in the anode projection zone than in the channels.

The initial bath velocity vectors are shown in Fig. 5. The maximal and mean velocities are 0.188 m s^{-1} and

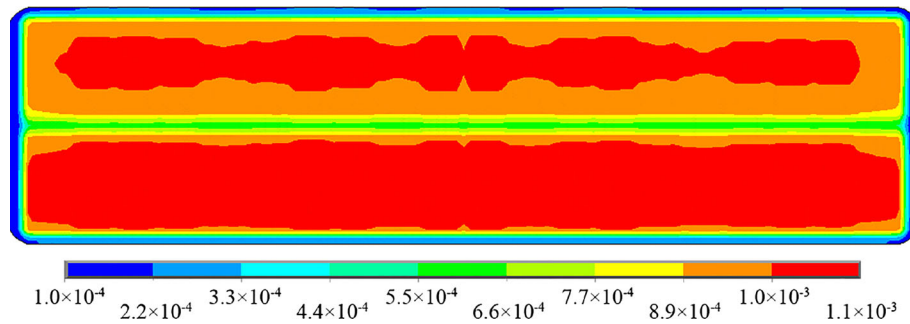


Fig. 4. Distribution of consumption rate of alumina on the bath bottom (Unit: $\text{kg s}^{-1} \text{m}^{-2}$).

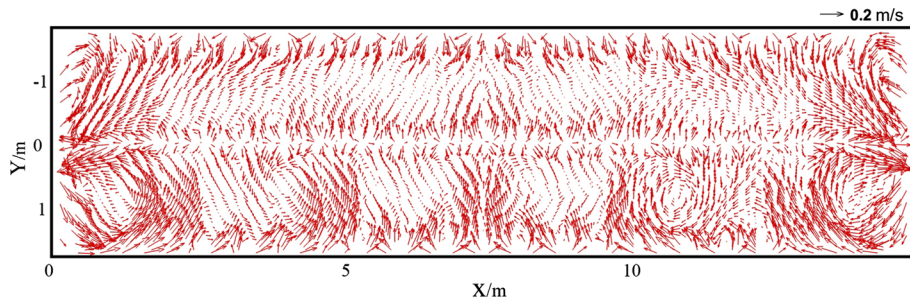


Fig. 5. Horizontal velocity vectors of bath.

0.058 m s^{-1} , respectively. There are some large vortexes in the upstream side and the corners, which are mainly induced by the EMFs. Meanwhile, a series of small eddies, stirred by the anode bubbles, is in the center and side channels.

Variation of Alumina Concentration Distribution with Time

With the multicomponent and multiphase flow model, the detailed alumina-mixing information can be obtained in the overall course. Take the first feeding circle for example, the distributions of alumina concentration every 10 s on the horizontal plane are shown in Fig. 6.

At the beginning, alumina aggregates around the feeding points, and the concentration remains the initial value for most other areas, as shown in Fig. 6a. Then, it starts to get dispersed in four streams around the anode corners, and the area with the highest alumina concentration moves away from the center channel (Fig. 6b and c). After 30 s, alumina diffuses within the whole cell, and the maximum concentration decreases from 3.7 wt.% to 2.8 wt.% in the end, as shown in Fig. 6d, e, and f. It can be seen in the above process that the alumina-mixing pattern is uneven; it is determined by the bath flow field form, which is shown as flow streams in Fig. 7. It also indicates that the alumina-mixing process has something to do with the stirring effect of vortexes. For example, near the anodes A5, A6, and A16, along with the rotary motion of bath, an arc-shaped alumina concentration distribution is formed.

Effects of Bubble and EMFs

As the bath flow is driven by the combined effects of anode bubble and EMFs, it is necessary to explore the inherent mechanism for the optimization of the mixing process. However, as both the two factors, EMFs and bubbles, contribute to the bath motion, their individual effects could not be analyzed without excluding one of them. Therefore, the mixing processes driven by bubbles and by EMFs are calculated, respectively, and the corresponding alumina concentration distributions on horizontal plane in the first feeding circle are, respectively, shown in Figs. 8 and 9 with an interval of 20 s.

Compared with the case in which only EMFs were considered, the alumina concentration distribution driven only by bubbles is highly symmetry along the center channel and the short axis, which is the same as Feng's^{17,18} results. Most of the added alumina gathers around the feeder points after being dispersed for 60 s, and the changes of maximum concentration on the discussed horizontal plane are relatively smooth. After feeding begins at $t = 5 \text{ s}$, the maximum value increases quickly to 3.7% at $t = 15 \text{ s}$, then it decreases gently to a normal level with the final value of 2.8%, as shown in Fig. 10a.

In contrast, the second case shows that EMFs strongly affect alumina dispersion. Although the natural diffusion rate is very low, alumina is still transported to most of the areas by the entrainment effect of bath bulks, as shown in Fig. 9. However, it is obvious that the bath flow cannot support a quick local dispersion, as those high-concentration bulks

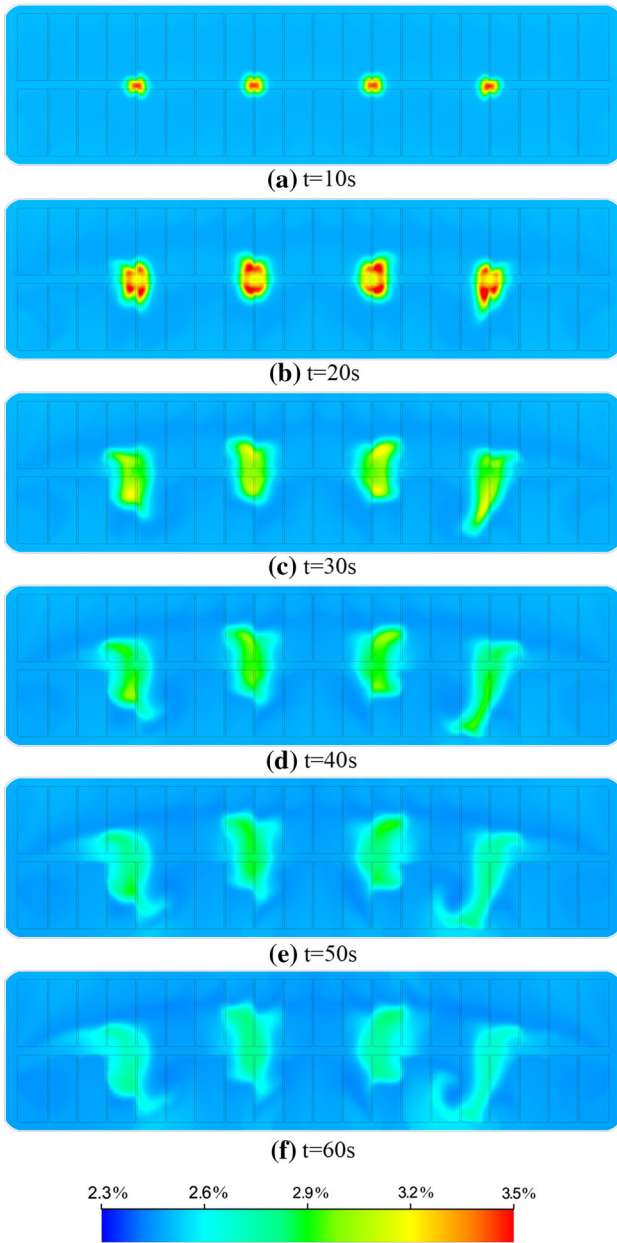


Fig. 6. Alumina concentration distribution on horizontal plane: (a) $t = 10$ s, (b) $t = 20$ s, (c) $t = 30$ s, (d) $t = 40$ s, (e) $t = 50$ s, and (f) $t = 60$ s.

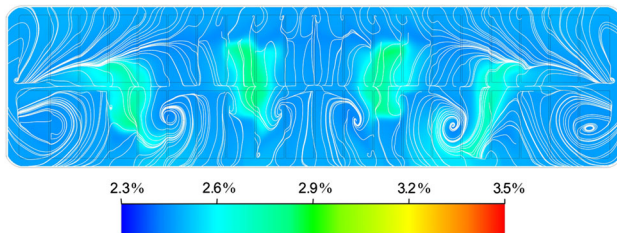


Fig. 7. Flow streams and alumina concentration distribution on horizontal plane.

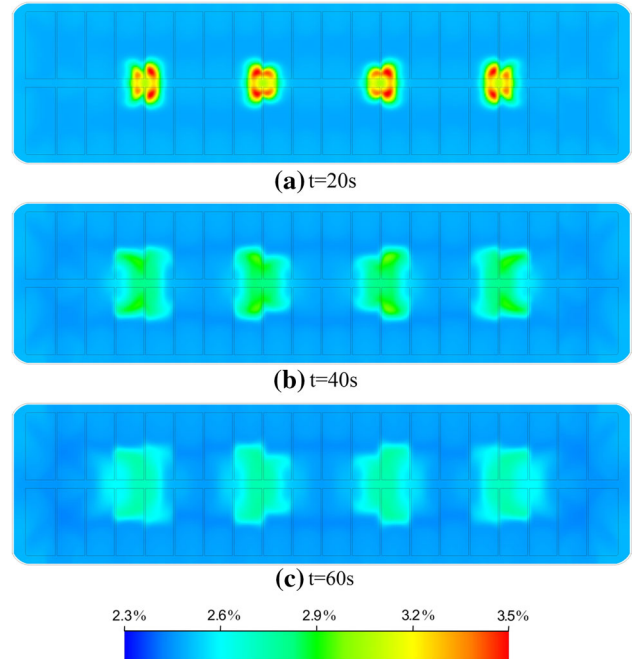


Fig. 8. Alumina concentration distribution on horizontal plane driven by only bubbles: (a) $t = 20$ s; (b) $t = 40$ s, and (c) $t = 50$ s.

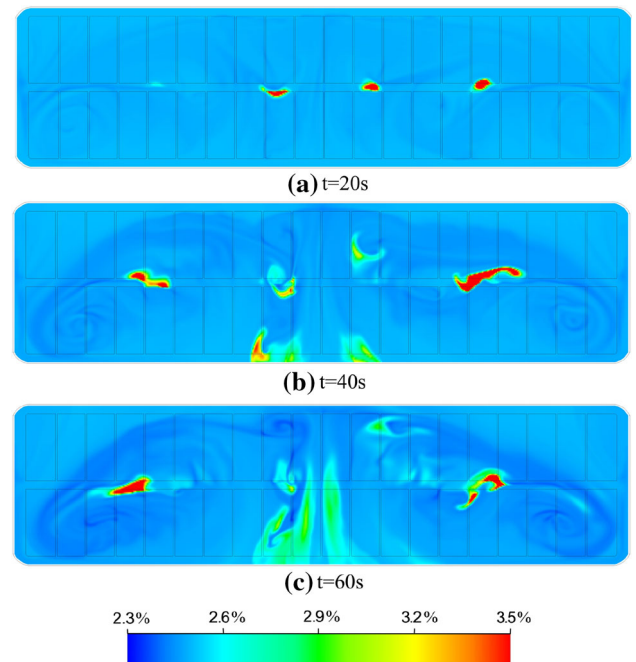


Fig. 9. Alumina concentration distribution on horizontal plane driven by only EMFs: (a) $t = 20$ s, (b) $t = 40$ s, (c) $t = 50$ s.

are maintained in very limited areas even it has experienced a journey from the feeding point to the bottom of the anode as seen from Fig. 9b and c. After the feeding actions begin at $t = 5$ s, the maximum value on the discussed horizontal plane also

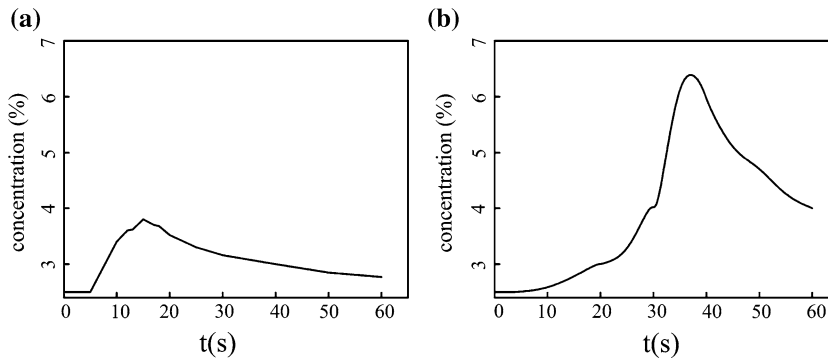


Fig. 10. Variation curve of maximum concentration on the discussed horizontal plane: (a) the effect of bubble and (b) the effect of EMFs.

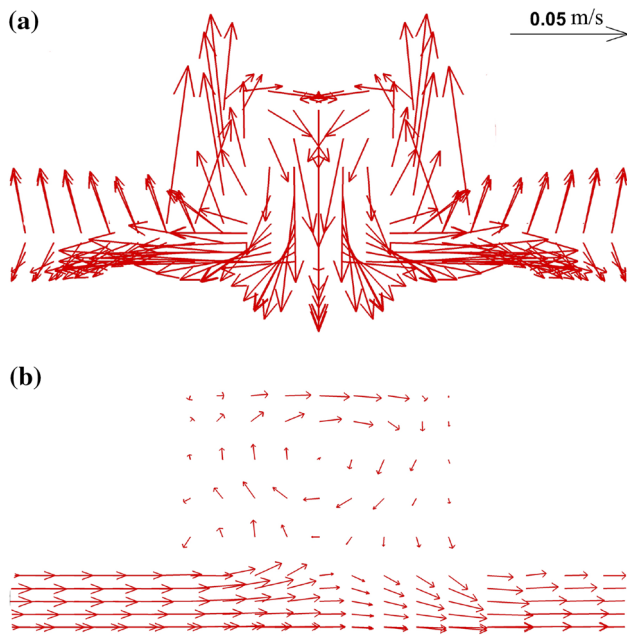


Fig. 11. Velocity vectors of bath in center channel: (a) the effect of bubble and (b) the effect of EMFs.

increases quickly. However, it takes 30 s to reach the extreme value of 6.7%, as shown in Fig. 10b, and the final value is 4% at the end of the first feeding cycle. If it takes place in an industrial cell, then the risk of sedimentation may increase because the saturation concentration of alumina in industrial cryolite is less than 8%.⁴

Another important difference between the effects of bubbles and of EMFs is that they have different ways of driving the bath flow. For example, after 20 s when the first feed point (the nearest to duct end) was fed, few alumina move to the observed plane under the first feeding point from the duct end, as shown in Fig. 9a. This is because vertical movements of the bath driven by EMFs in the narrow center channel formed a local vortex circulation so that the small vertical component of bath flow limits the transportation of alumina from the feed point to the ACD spaces. The flow fields in center

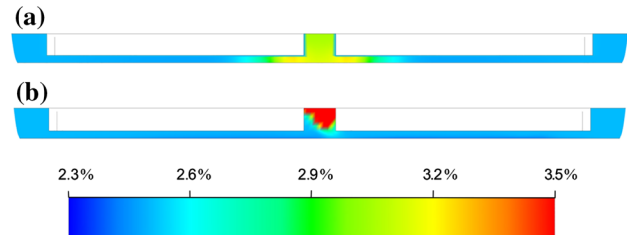


Fig. 12. Alumina concentration distribution on vertical plane: (a) the effect of bubble and (b) the effect of EMFs.

channel below the first feed point for the two cases are shown in Fig. 11. The results of alumina concentration distribution after 15 s dispersion are shown as Fig. 12. It is clearly illustrated that the bubble has a greater effect on vertical transportation in the early mixing stage, while the alumina are gathered in the upper center channel if the bubble is excluded. Besides, the horizontal flow of bath is observed under the anode in the EMFs case, as shown in Fig. 11b. This is the reason why alumina is transported to most of the cell areas by the bath movement induced by EMFs. The average velocity of the bath in the upper center channel in the bubble case is 0.043 m s^{-1} , which is much faster than the value of 0.017 m s^{-1} in the EMFs case. It may be one of the reasons contributing to the faster transportation of alumina induced by the bubble. Therefore, the bubble breaks up the agglomerated bulks of alumina and speeds up the mixing in the local areas rather than driving the alumina-contained bath to the whole cell area, which is dominated by the EMFs.

Thus, the whole mixing process can be described as follows: Once alumina is fed into the surface layer of the bath as agglomerated bulks in the center channel, it starts to descend to the ACD areas mostly by the stirring effects of bubble movement. In the descending process, the alumina bulks are rapidly broken up when collided with bubbles. Then, with the combined driving forces, alumina entrained in bath disperses to all cell areas through horizontal flow dominated by EMFs. And bubbles still play the most important role in local distribution of alumina.

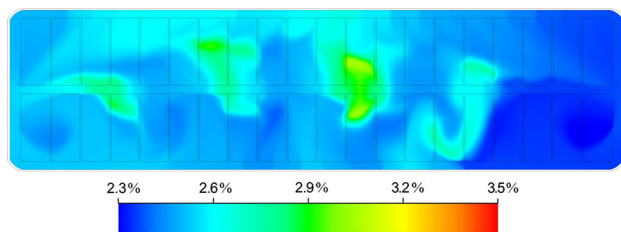


Fig. 13. Alumina concentration distribution on horizontal plane (at the end of the seventh feeding circle).

At last, alumina is dissolved and consumed in the electrochemical reacting area. As an extension of the model, at the end of the seventh feeding circle, alumina concentration distributions on horizontal plane are shown in Fig. 13. Contrasting Fig. 6f to Fig. 13, the results show that most areas keep a slightly fluctuated alumina concentration, but apparently, less alumina goes to the tap end than other areas.

Admittedly, the local alumina consumption depends on the online current, and it is reported that the gas bubbles can have rather complex behavior in the bath movement, which may have some different impacts on the bath flow. These factors are not considered in the model presented in this article, and it can be regarded as further work on the issues of alumina mixing, which needs to be studied in the future.

CONCLUSION

In this article, an extended CFD model was carried out to investigate the mixing process of alumina in aluminum reduction cells. The following conclusions were derived:

1. The influence of electromagnetic field and anode gas bubble were considered in the model. Besides, the simulated practical feeding regime was involved and the consuming rate of alumina was decided by the local current intensity on the bath-metal interface.
2. The alumina-mixing process in a 300-kA cell was calculated using the established model. The alumina distribution pattern is uneven but is determined by the bath flow field.
3. The effects of bubbles and EMFs on the alumina-mixing process were calculated, respectively. The movement of the bubbles makes alumina disperse more quickly in local areas than in the global region. The EMF plays a significant role in long-range transportation of alumina in the cell. Each of the two forces should be taken into consideration in modeling since both of them have positive effects on distribution uniformity and dispersion rate of alumina added into the cell.

ACKNOWLEDGEMENTS

The authors are grateful for the financial support of the National Natural Science Foundation of China (51274241 and 51104187), and the Fundamental Research Funds for the Central Universities of Central South University (2014zzts027).

REFERENCES

1. J. Thonstad, P. Fellner, G.M. Haarberg, J. Híveš, H. Kvande, and V. Sterten, *Aluminum Electrolysis*, 3rd ed. (Düsseldorf, Germany: Aluminium-Verlag Marketing & Kommunikation GmbH, Breuerdruck, 2010), pp. 295–310.
2. K.A. Paulsen, J. Thonstad, S. Rolseth, and T. Ringstad, *Light Metals 1993*, ed. S.K. Das (Warrendale, PA: TMS, 1993), pp. 233–238.
3. G.I. Kuschel and B.J. Welch, *Light Metals 1991*, ed. E.R. Cutshall (Warrendale, PA: TMS, 1991), pp. 229–305.
4. A. Solheim, S. Rolseth, E. Skybakmoen, L. Støen, Å. Sterten, and T. Støre, *Light Metals 1995*, ed. J.W. Evans (Warrendale, PA: TMS, 1995), pp. 451–460.
5. B. Moxnes, A. Solheim, M. Liane, E. Svinsås, and A. Halkjelsvik, *Light Metals 2009*, ed. G. Bearne (Warrendale, PA: TMS, 2009), pp. 461–466.
6. R. Keller, *Light Metals 2005*, ed. H. Kvande (Warrendale, PA: TMS, 2005), pp. 147–150.
7. G. Tarcy and A. Taberaux, *Light Metals 2011*, ed. S. Lindsay (Warrendale, PA: TMS, 2011), pp. 329–332.
8. C.Y. Cheung, C. Menictas, J. Bao, M. Skyllas-Kazacos, and B.J. Welch, *Ind. Eng. Chem. Res.* 52, 9632 (2013).
9. K.Å. Rye, I. Solberg, T. Eidet, and S. Rolseth, *Light Metals 2001*, ed. J.L. Anjier (Warrendale, PA: TMS, 2001), pp. 529–533.
10. W.E. Wahnsiedler, *Light Metals 1987*, ed. R.D. Zabreznik (Warrendale, PA: TMS, 1987), pp. 269–287.
11. S.D. Lympny, D.P. Ziegler, and J.W. Evans, *Light Metals 1983*, ed. E.M. Adkins (Warrendale, PA: TMS, 1983), pp. 507–517.
12. M. Segatz, *Light Metals 1993*, ed. S.K. Das (Warrendale, PA: TMS, 1993), pp. 355–360.
13. T. Haarberg, A. Solheim, S.T. Johansen, and P.A. Solli, *Light Metals 1998*, ed. B.J. Welch (Warrendale, PA: TMS, 1998), pp. 475–481.
14. O. Kobbeltvedt and B.P. Moxnes, *Light Metals 1997*, ed. H. Reidar (Warrendale, PA: TMS, 1997), pp. 369–376.
15. Y.F. Wang, L.F. Zhang, and X.J. Zuo, *Metall. Mater. Trans. B* 42B, 1051 (2011).
16. D.C. Chesonis, S.T. Johansen, S. Rolseth, and J. Thonstad, *J. Appl. Electrochem.* 19, 703 (1989).
17. Y.Q. Feng, M.A. Cooksey, and M.P. Schwarz, *Light Metals 2010*, ed. A.M. Hagni (Warrendale, PA: TMS, 2010), pp. 451–456.
18. Y.Q. Feng, M.A. Cooksey, and M.P. Schwarz, *Light Metals 2011*, ed. J. Lindsay (Warrendale, PA: TMS, 2011), pp. 543–548.
19. J. Li, Y.J. Xu, H.L. Zhang, and Y.Q. Lai, *Int. J. Multiph. Flow* 37, 46 (2011).
20. D.S. Severo, A.F. Schneider, E.C.V. Pinto, V. Gusberti, and V. Potocnik, *Light Metals 2005*, ed. H. Kvande (Warrendale, PA: TMS, 2005), pp. 475–480.
21. J. Li, W. Liu, Y.Q. Lai, Q.Y. Li, and Y.X. Liu, *Acta Metall. Sinica* 19, 105 (2006).
22. O. Kobbeltvedt, S. Rolseth, and J. Thonstad, *Light Metals 1996*, ed. W. Hale (Warrendale, PA: TMS, 1996), pp. 421–427.
23. J. Li, W. Liu, Y.Q. Lai, and Y.X. Liu, *JOM* 60, 58 (2008).
24. L. Cassayre, T.A. Utigard, and S. Bouvet, *JOM* 54 (5), 41 (2002).